Nanoscale

PAPER

Cite this: *Nanoscale*, 2015, **7**, 12205

Engineering of parallel plasmonic–photonic interactions for on-chip refractive index sensors†

Linhan Lin and Yuebing Zheng*

Ultra-narrow linewidth in the extinction spectrum of noble metal nanoparticle arrays induced by the lattice plasmon resonances (LPRs) is of great significance for applications in plasmonic lasers and plasmonic sensors. However, the challenge of sustaining LPRs in an asymmetric environment greatly restricts their practical applications, especially for high-performance on-chip plasmonic sensors. Herein, we fully study the parallel plasmonic–photonic interactions in both the Au nanodisk arrays (NDAs) and the core/shell SiO_2/Au nanocylinder arrays (NCAs). Different from the dipolar interactions in the conventionally studied orthogonal coupling, the horizontal propagating electric field introduces the out-of-plane "hot spots" and results in electric field delocalization. Through controlling the aspect ratio to manipulate the "hot spot" distributions of the localized surface plasmon resonances (LSPRs) in the NCAs, we demonstrate a high-performance refractive index sensor with a wide dynamic range of refractive indexes ranging from 1.0 to 1.5. Both high figure of merit (FOM) and high signal-to-noise ratio (SNR) can be maintained under these detectable refractive indices. Furthermore, the electromagnetic field distributions confirm that the high FOM in the wide dynamic range is attributed to the parallel coupling between the superstrate diffraction orders and the height-induced LSPR modes. Our study on the near-field "hot-spot" engineering and far-field parallel coupling paves the way towards improved understanding of the parallel LPRs and the design of high-performance on-chip refractive index sensors.

Received 14th May 2015,
Accepted 10th June 2015

DOI: 10.1039/c5nr03159a

www.rsc.org/nanoscale

Introduction

Various Au or Ag nanostructures have been widely studied in fluorescence enhancement,[1–3] photovoltaics,[4–7] bio-sensing,[8–17] and cancer phototherapy[18,19] due to their characteristic optical responses supported by the localized surface plasmon resonances (LSPRs),[20–23] which originate from the light-induced coherent oscillation of surface electrons. When these nanoparticles are placed in close proximity, interactions between the particles will take place and the hybrid modes can be generated.[24] Specifically, when the particles are placed in the regularly distributed arrays with the period comparable to the wavelength of the incident light, the light-particle interaction causes multiple scattering and leads to propagating waves in the plane of the nanoparticle arrays, which are known as the diffraction waves. Once the wavelength of the diffraction waves overlaps with the resonance wavelength of the LSPRs, a strong coherent interaction dramatically modifies the optical responses of the nanoparticle arrays, which is called lattice plasmon resonances (LPRs) or collective resonances.[25–33]

The collective behavior of these nanoparticle arrays was mathematically demonstrated using the coupled dipole (CD) method.[34–39] Each nanoparticle is treated as a dipole with $\boldsymbol{P}_i = \alpha_i \boldsymbol{E}_i$, in which α_i is the polarizability of the ith particle, and $\boldsymbol{E}_i$ is the sum of the incident field and the retarded field of the other particles at the location of the i^{th} particle. In the infinite arrays of particles, the polarizability of each particle is the same, and the effective polarizability of each nanoparticle and the extinction cross section can be written as

$$\alpha_{\text{eff}} = \frac{1}{(1/\alpha_{\text{s}} - S)} \quad (1)$$

and

$$C_{\text{ext}} = 4\pi N k \ \text{Im}(\alpha_{\text{eff}}) \quad (2)$$

where α_{s} is the polarizability of an isolated particle, S is the sum of retarded dipoles from other particles, N is the number of particles in the arrays, and k is the wave number of the incident light. When S equals to $1/\alpha_{\text{s}}$, the extinction cross section is infinite and the resonance takes place. This model predicts a sharp and narrow linewidth in the Au or Ag nanoparticle arrays, which is caused by the suppression of radiative

Department of Mechanical Engineering, Materials Science & Engineering Program, and Texas Materials Institute, The University of Texas at Austin, Austin, TX 78712, USA. E-mail: zheng@austin.utexas.edu

†Electronic supplementary information (ESI) available. See DOI: 10.1039/c5nr03159a

damping. The narrow linewidth is attractive for the applications of the arrays in plasmonic lasers,[40–42] and plasmonic sensors with an improved figure of merit (FOM).[43–48]

However, the generation of LPRs requires a homogeneous environment to support the plasmonic–photonic coupling between the LSPRs and the diffraction orders, which makes it difficult to experimentally obtain the LPRs for the on-chip plasmonic sensors due to the presence of the substrate, which cuts off the diffraction orders at the interface.[49] This problem is usually solved by introducing an index matching layer on the top of the particles to achieve a quasi-symmetric environment.[25,26] However, this has greatly restricted the sensing applications because the detectable refractive index of the target analytes is limited, which was close to that of the substrates.[43,44,48] Therefore, the high FOM is maintained in a narrow effective range of detected refractive indices. Beyond this range, the plasmonic–photonic coupling becomes weak or even vanishes, and the FOM will be determined by the LSPRs instead, whose FOM is not more than 5 as reported.[50] So far, it has been challenging to develop the plasmonic sensors with both a high FOM and a wide working range of refractive indices. Another system based on the coupling between the surface plasmon polaritons (SPPs) and the diffraction orders in the metallic nanohole arrays has been demonstrated to achieve the high FOM in the refractive index sensors. However, the signal-to-noise ratio (SNR) in such a system (−23 dB)[51] is much lower than that in the LPR-based sensors due to the capability of the latter to confine light at the subwavelength scale with highly concentrated electromagnetic fields and the strong optical response.

A recent study of the parallel coupling in the Au nanoparticle arrays has shown that a narrow linewidth exists in the extinction spectra when the LSPRs couple with the superstrate diffraction orders, revealing its potential applications for the high-FOM sensors.[29,52] The coupling mechanism in the parallel coupling is still unclear and no study has been carried out on the application of parallel coupling in refractive index sensing. In this paper, we apply finite-difference time-domain (FDTD, Lumerical Inc.) simulations to comparatively study the parallel plasmonic–photonic coupling in the two-dimensional (2D) Au nanodisk arrays (NDAs) and core/shell SiO_2/Au nanocylinder arrays (NCAs) for the sensing applications. We managed to address three questions in this paper: (1) What is the difference between the orthogonal coupling and parallel coupling? (2) How to achieve a refractive index sensor with a wide working range of refractive indices based on parallel coupling? (3) How to maintain a high FOM in a wide range of working refractive indices? We expect that the study in this paper can be helpful for an improved understanding of the plasmonic–photonic coupling mechanism and the design of high-performance refractive index sensors.

Results and discussion

Orthogonal and parallel coupling in the Au NDAs

Most of the work in the LPMs was carried out in the Au NDAs with $a_{\parallel} = a_{\perp}$,[26,30,42,48] which makes the coupling mechanism unclear and the origins of the enhanced "hot spot" locations and intensity inscrutable. In order to reveal the different coupling behaviors of the Au nanoparticle arrays, both orthogonal and parallel couplings in the Au NDAs are simulated here. Fig. 1a schematically displays the structure of the Au NDAs and the different photonic diffraction orders, or the Rayleigh Anomalies (RA), which is due to the passing-off of a spectral diffraction order when it grazes the surface of the gratings or the nanoparticle arrays. Orthogonal and parallel couplings are achieved when the polarization of the incident light is vertical or parallel to the propagation direction of the diffraction waves, respectively. With *x*-polarized light, the (0, ±1) diffraction orders were generated by tuning $a_{\perp}$ to scatter the incident light along the *y*-axis in the *xy* plane, with two lobes in the H_z components distributed in a unit cell. The standing waves with alternating positive and negative H_z components result from the in-plane scattering after the light–particle interactions and the interference from the travelling waves in opposite directions. These diffraction waves couple with the plasmonic "hot spots" on both sides of the nanodisks and enhance the dipole intensity as predicted by the CD theory. The number of lobes in a unit cell depends on the diffraction orders, *i.e.*, the second diffraction orders would show four lobes in a unit cell. According to the dual principle, the (±1, 0) diffraction orders are generated by tuning $a_{\parallel}$ to scatter the incident light along the *x*-axis in the *xy* plane, and the two lobes in the E_z components are observed. In contrast to the orthogonal coupling, the E_z component cannot couple with the dipolar "hot spots" because of the different oscillation directions. Instead these E_z components couple with the out-of-plane "hot spots" at the top of the nanodisks as shown in Fig. 1a. For normal incidence, the wavelength of the diffraction orders can be determined when the out-of-plane wave number ($k^{\perp}_{i,j}$) becomes zero.

$$k^{\perp}_{i,j} = \sqrt{\left(n\frac{2\pi}{\lambda}\right)^2 - {k^{\parallel}_{i,j}}^2} = 2\pi\sqrt{\frac{n^2}{\lambda^2} - \frac{i^2}{{a_x}^2} - \frac{j^2}{{a_y}^2}} \qquad (3)$$

where n is the refractive index of the media surrounding the structure, λ is the wavelength of incident light in vacuum, $k^{\parallel}_{i,j}$ is the in-plane wavelength number, a_x and a_y indicate the lattice constants along the x and y axis, which corresponds to $a_{\parallel}$ and $a_{\perp}$ indicated in Fig. 1, and i and j are the integers which determine different diffraction orders. The crossover from an imaginary to a real value of $k^{\perp}_{i,j}$ causes a transition from evanescent to radiative order, allowing the far-field radiative interaction between the nanoparticles.

The transmission spectra of the Au NDAs with a diameter of 240 nm, height of 70 nm, $a_{\parallel}$ = 400 nm and $a_{\perp}$ ranging from 400 to 1200 nm are shown in Fig. 1b, which reveal the orthogonal coupling behavior. $a_{\parallel}$ = 400 nm is adopted here to avoid the parallel coupling. When the (0, ±1) substrate diffraction orders $\lambda^{sub}_{(0,\pm1)}$ cross the resonance peak of the single nanodisk, a sharp and narrow transmission dip is obtained, which confirms the strong plasmonic–photonic coupling and the dramatically improved extinction efficiency. A weak interaction

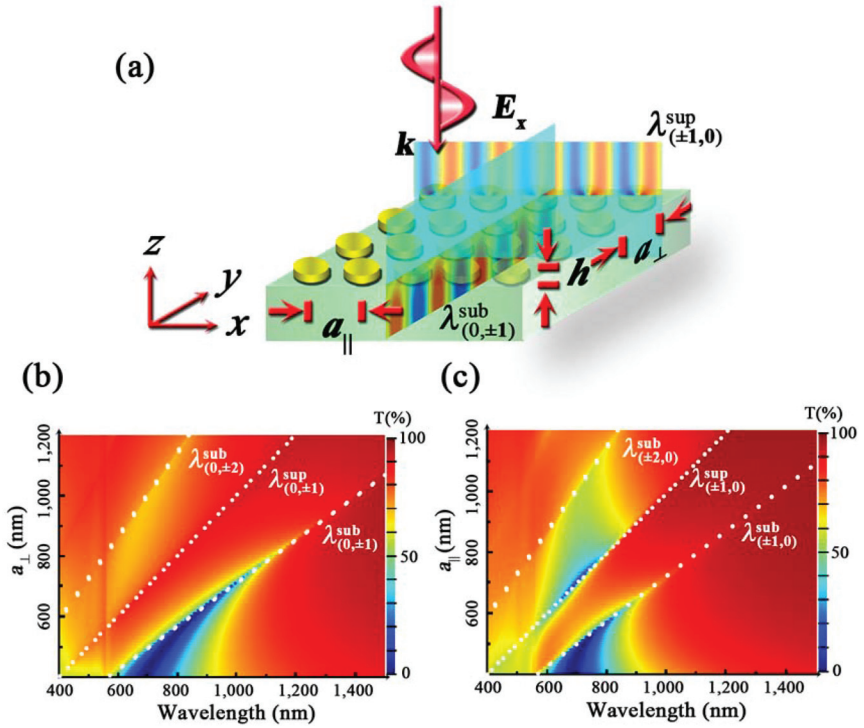

Fig. 1 Orthogonal and parallel couplings in the Au NDAs. Schematic of the Au NDAs when the LSPRs couple (a) orthogonally with $\lambda^{sub}_{(\pm1,\ 0)}$ and parallelly with $\lambda^{sup}_{(\pm1,\ 0)}$, respectively. The diameter of the Au nanodisks is fixed at 240 nm. $a_{\perp}$ and $a_{\parallel}$ indicate the lattice constants that are vertical and parallel to the polarization of the incident light, respectively. h is the height of the nanodisks (70 nm). The x-polarized light is launched from the top of the NDAs. The cross sections show the real part of Hz for $\lambda^{sub}_{(\pm1,\ 0)}$ and the real part of E_z for $\lambda^{sup}_{(\pm1,\ 0)}$ through the center of the nanodisks, respectively. The simulated transmission spectra for the Au NDAs with the lattice constants of (b) $a_{\parallel}$ = 400 nm, $a_{\perp}$ ranging from 400 nm to 1200 nm and (c) $a_{\perp}$ = 400 nm, $a_{\parallel}$ ranging from 400 nm to 1200 nm. The diffraction orders are indicated as dotted lines.

between $\lambda^{sub}_{(0,\ \pm2)}$ and the LSPR is also observed here. However, no orthogonal coupling takes place between the (0, ±1) superstrate diffraction order $\lambda^{sup}_{(0,\ \pm1)}$ and the LSPR. A similar coupling behavior between the LSPR and the substrate diffraction orders is observed for the parallel coupling (Fig. 1c). However, an additional coupling between the (±1, 0) superstrate diffraction order $\lambda^{sup}_{(\pm1,\ 0)}$ and the LSPR is obtained. Two transmission dips co-exist when $a_{\parallel}$ changes from 600 nm to 800 nm, which is attributed to the coupling between the LSPR and two different diffraction orders, respectively, *i.e.*, $\lambda^{sup}_{(\pm1,\ 0)}$ for the shorter wavelength dip and $\lambda^{sub}_{(\pm1,\ 0)}$ for the one at longer wavelength. It should be noted that the parallel coupling cannot be simply explained by the CD model, in which the polarization of the incident light is vertical to the propagation direction of the diffraction waves. In order to gain an insight into the difference between the orthogonal and parallel coupling, the electromagnetic field distributions are examined.

Electromagnetic field distributions in Au NDAs

Fig. 2a–f demonstrate the plasmonic–photonic coupling in the electromagnetic field distributions for different configurations. Due to the dipolar interaction, the orthogonal coupling greatly enhances the near-field intensity, as shown in Fig. 2a and b. Therefore, the "hot spots" on both sides of the nanodisk exhibit enhanced intensity compared with the isolated Au nanodisk. The in-plane propagating magnetic field, which is enhanced by the scattering of each nanodisk in the arrays, is responsible for the diffraction orders. This propagating magnetic field introduces a retarded electric field with the polarization consistent with the incident electric field (x-polarized), enhancing both the intensity of the near-field "hot spots" and the extinction efficiency. Fig. 2c and d show the field distributions when the LSPR is coupled with $\lambda^{sub}_{(\pm1,\ 0)}$. In contrast, the intensity of E_x is much lower than that of the orthogonal LPR, indicating that the parallel coupling does not arise from the dipolar interaction among the nanodisks. In addition, a delocalization of the total electric field intensity is revealed in Fig. 2d, where the "hot spots" at the bottom of the nanodisk couple with the enhanced in-plane propagating electric field. Fig. 2e and f show the field distributions when the LSPR is coupled with $\lambda^{sup}_{(\pm1,\ 0)}$. Besides the "hot spots" at the interfaces between the nanodisks and the substrate, an additional pair of "hot spots" at the top side of the nanodisks is observed in the $|E_x|^2$ distribution (Fig. 2e). The delocalization of electric field into the superstrate confirms the energy transfer between the near-field "hot spots" and the far-field photonic diffraction orders (Fig. 2f). These different near-field electromagnetic distributions between the orthogonal and parallel couplings are

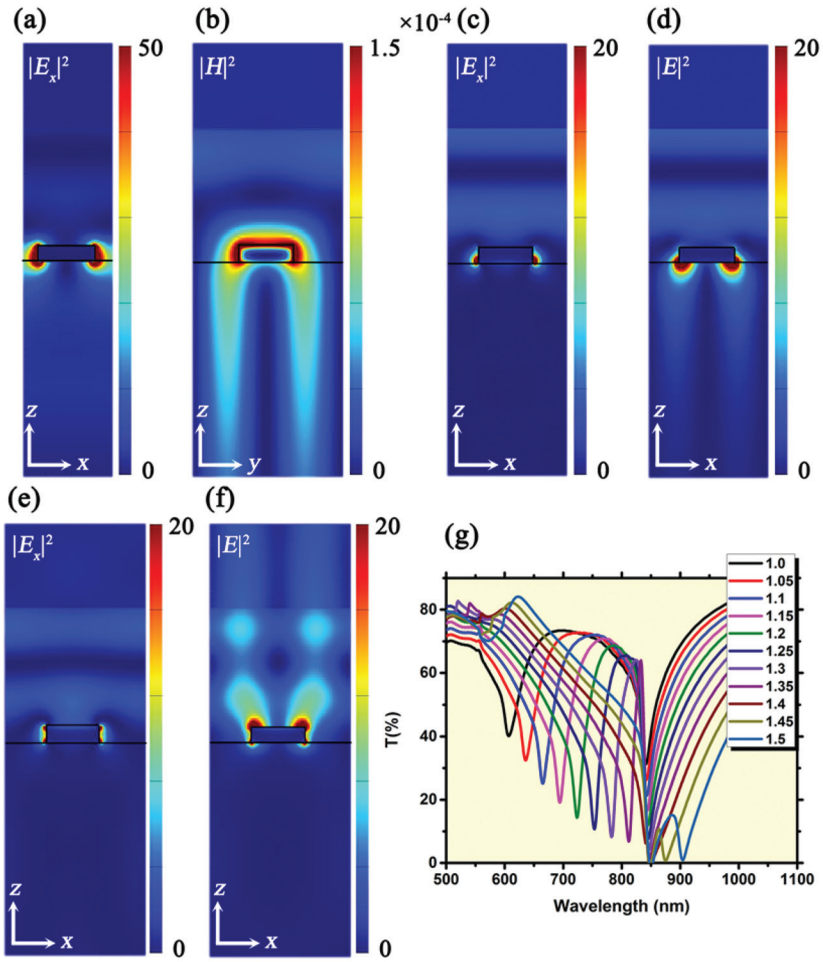

Fig. 2 (a)–(f) Distributions of $|E|^2$ and $|E_x|^2$ in the *xz* plane and $|H|^2$ in the *yz* plane through the center of the nanodisk. The Au NDAs have a diameter of 240 nm, height of 70 nm, (a) and (b) $a_{\parallel}$ = 400 nm, $a_{\perp}$ = 670 nm, λ = 940 nm, (c) and (d) $a_{\perp}$ = 400 nm, $a_{\parallel}$ = 540 nm, λ = 762 nm, (e) and (f) $a_{\perp}$ = 400 nm, $a_{\parallel}$ = 660 nm, λ = 662 nm. (g) The transmission spectra of the Au NDAs as a function of the superstrate refractive index, which is changed from 1.0 to 1.5. The NDAs have lattice constants of $a_{\perp}$ = 400 nm and $a_{\parallel}$ = 600 nm.

caused by the different electromagnetic field components in the diffraction orders. Instead of H_z as in the case of orthogonal LPRs, the in-plane propagating E_z in parallel LPRs directly introduces the out-of-plane oscillations of the surface electrons, leading to the out-of-plane "hot spots" as shown in Fig. 2d and f. When $\lambda^{sub}_{(\pm1,\ 0)}$ or $\lambda^{sup}_{(\pm1,\ 0)}$ overlaps with the resonance wavelength of the LSPRs, both the in-plane scattering and the intensity of the diffraction orders are enhanced. Furthermore, due to the collective interactions between these out-of-plane "hot spots" and the radiative diffraction orders, the intensity of the out-of plane "hot spots" is much higher than that of the LSPRs as confirmed in Fig. 2.

Refractive index sensing in the Au NDAs

According to eqn (3), $\lambda^{sup}_{(\pm1,\ 0)}$ is proportional to the superstrate refractive index, implying the possibility of developing the plasmonic sensors based on the parallel coupling. To estimate the sensing performance of the Au NDAs, we simulated the transmission spectra of the Au NDAs with $a_{\perp}$ = 400 nm and $a_{\parallel}$ = 600 nm as a function of the superstrate refractive index (Fig. 2g). The two transmission dips at 600 nm and 850 nm are attributed to the parallel LPRs associated with $\lambda^{sup}_{(\pm1,\ 0)}$ and $\lambda^{sub}_{(\pm1,\ 0)}$, respectively. Because $\lambda^{sub}_{(\pm1,\ 0)}$ is independent of the superstrate refractive index, the dip at 850 nm remains unchanged when the superstrate refractive index is increased. The improved extinction efficiency is due to the reduced difference in the refractive index between the superstrate and the substrate. However, the LPR at 600 nm is highly sensitive to the superstrate refractive index, with a wavelength sensitivity of 588 nm per refractive index unit (RIU). Taking the full width at half maximum (FWHM) at a refractive index of 1.2, a FOM of 13.07 is obtained, which is much higher than the FOM of single nanoparticles. However, the linewidth in the transmission spectra of the Au NDAs is still too broad for the high-performance sensors. Next, we propose the new structure, *i.e.*, core/shell SiO_2/Au NCAs, to further reduce the linewidth and enhance the FOM in the wide dynamic range.

Parallel coupling in core/shell NCAs

In order to improve the FOM of the plasmonic sensors based on the parallel coupling, one needs to eliminate the interaction between the substrate and the plasmonic–photonic coupling.[53,54] Here, we propose to employ the core/shell SiO_2/Au NCAs to manipulate the plasmonic "hot spots" in the nanocylinders (NCs) in a way that they will be shifted away from the substrates to minimize the interactions, which both narrow the linewidth and increase the sensitivity to superstrate refractive index for an enhanced FOM. The NCAs are schematically illustrated in Fig. 3a. The diameter of the NC core is fixed at 200 nm and the thickness of the Au shell is 20 nm, resulting in a total diameter of 240 nm. The height of the NCs changes from 50 nm to 400 nm to increase the height-to-diameter aspect ratio. $a_\perp$ = 400 nm is fixed and $a_\parallel$ is varied from 400 to 1200 nm in order to observe the parallel coupling behavior in the NCAs.

The transmission spectra as a function of the wavelength and $a_\parallel$ are displayed in Fig. 3b–e, where the height of the NCs is changed from 100 to 400 nm. The NCAs with a height of 50 nm show similar transmission spectra as that of the Au NDAs (see Fig. S1 in the ESI†). The LSPR at 950 nm (indicated as the D_1 mode in Fig. 3b–e), which is a dipole bonding mode with the "hot spots" located at the interface between the NCs and the substrate, is similar to that in the Au NDAs. However, the interaction between the charges in the inner and outer parts of the Au nanoshells causes the redshift of the resonance wavelength. The increase of height introduces another dipole bonding mode (D_2 mode) and a quadrupole mode (Q modes),[32] which promotes the "hot spots" toward the upper side of the NCs (see Fig. 4a and c). In contrast to the D_1 mode, these height-induced modes are sensitive to the variation of the height, *i.e.*, the resonance wavelength redshifts when the height increases.

Parallel plasmonic–photonic coupling between the height-induced LSPRs and $\lambda^{sup}_{(\pm1,\ 0)}$ is observed. In Fig. 3b and c, $\lambda^{sup}_{(\pm1,\ 0)}$ begins to couple with the D_2 mode at $a_\parallel$ = 600 nm, and a further increase of $a_\parallel$ leads to the coupling between $\lambda^{sup}_{(\pm1,\ 0)}$ and the D_1 mode. As shown in Fig. 3d and e, a co-coupling between $\lambda^{sup}_{(\pm1,\ 0)}$ and two modes of LSPRs occurs, *i.e.*, $\lambda^{sup}_{(\pm1,\ 0)}$ couples with both the D_1 and D_2 modes because the D_2 mode partially overlaps with the D_1 mode. This is confirmed in the electromagnetic field distributions as discussed in the next sub-section. The Q mode located at the shorter wavelength could also weakly couple with $\lambda^{sup}_{(\pm1,\ 0)}$ (Fig. 3d), and this coupling strengthens when the height of the NCAs is further increased (Fig. 3e). It should be noted that the behavior of parallel coupling between these LSPRs and $\lambda^{sup}_{(\pm1,\ 0)}$ is quite different from that of orthogonal coupling. For the latter, $\lambda^{sup}_{(0,\ \pm1)}$ can only couple with the D_2 mode and no coupling between $\lambda^{sup}_{(0,\ \pm1)}$ and the D_1/Q mode is obtained.[32]

Electromagnetic field distributions in the core/shell NCAs

We further study the electromagnetic field distributions to better understand the parallel coupling in the NCAs. Fig. 4a shows the near-field distributions of $|E_x|^2$ for the Q mode, in

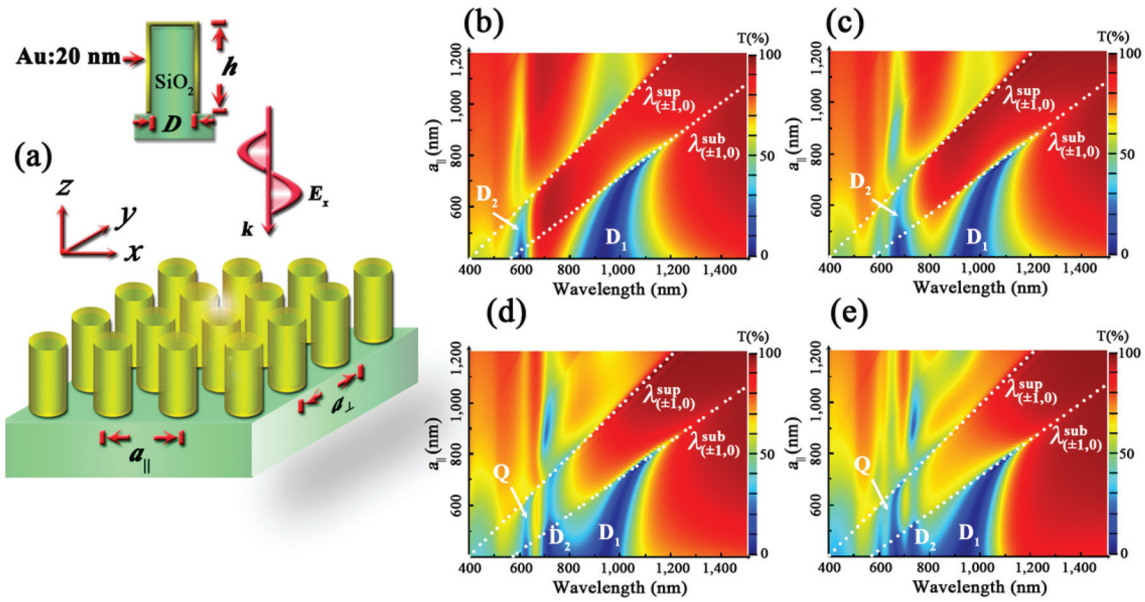

Fig. 3 (a) Schematic of the core/shell SiO_2/Au NCAs. The diameter of the NCs is fixed at 200 nm, $a_\perp$ and $a_\parallel$ indicate the lattice constants that are vertical and parallel to the polarization direction of the incident light, respectively. h is the height of the NCs, which ranges from 50 to 400 nm. The thickness of the Au shell is 20 nm. The x-polarized light is launched from the top of the NCAs. The inset in (a) shows the cross section of a single core/shell NC. (b)–(e) The simulated transmission spectra of the NCAs as a function of $a_\parallel$, which ranges from 400 nm to 1200 nm. The NCAs have the lattice constants of $a_\perp$ = 400 nm and (b) h = 100 nm, (c) h = 200 nm, (d) h = 300 nm, (e) h = 400 nm. The parallel diffraction orders $\lambda^{sub}_{(\pm1,\ 0)}$ and $\lambda^{sup}_{(\pm1,\ 0)}$ are indicated with the dotted lines.

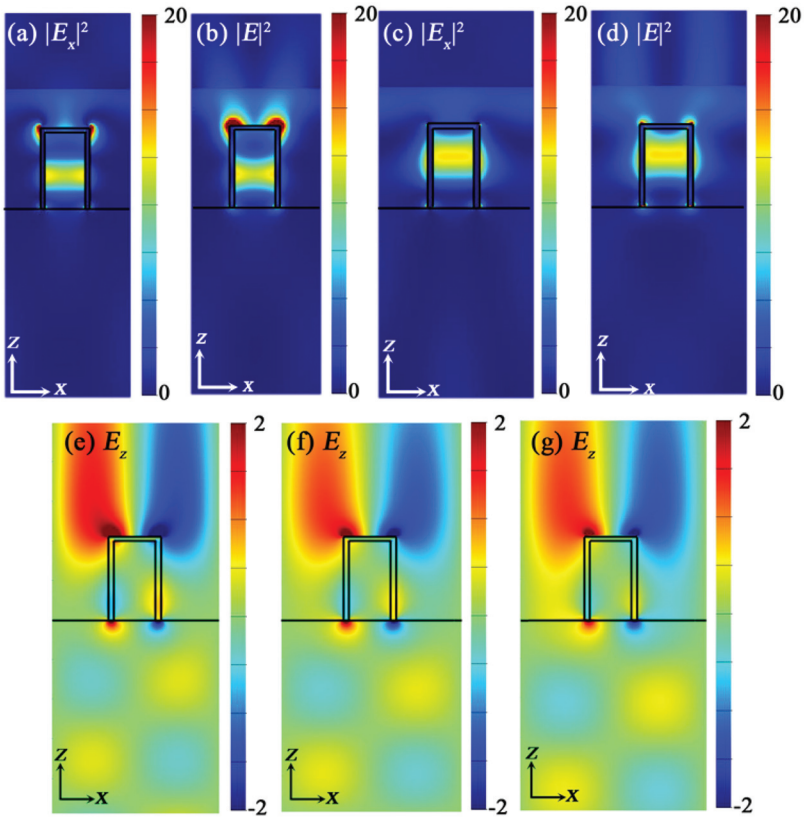

Fig. 4 Distributions of $|E_x|^2$, $|E|^2$ and the real part of E_z in the *xz* plane through the center of the NCs. The NCAs have D = 200 nm, h = 400 nm, $a_\perp$ = 400 nm (a) and (b) $a_\parallel$ = 650 nm, λ = 644 nm, (c) and (d) $a_\parallel$ = 750 nm, λ = 752 nm, (e) $a_\parallel$ = 800 nm, λ = 796 nm, (f) $a_\parallel$ = 850 nm, λ = 840 nm, (g) $a_\parallel$ = 900 nm, λ = 888 nm.

which a quadrupole pattern is observed. In the $|E|^2$ distribution (Fig. 4b), the "hot spots" in the outer parts of the NCs couple with $\lambda^{sup}_{(\pm1,\ 0)}$ and the new "hot spots" at the top of the NCs are linked with the two lobes in the superstrate. Fig. 4c and d reveal the coupling between the dipole at the outer shells on the sides of the NCs (D_2 mode) and $\lambda^{sup}_{(\pm1,\ 0)}$. It should be noted that for both D_2 and Q modes, only the "hot spots" at the outer shells can couple with the diffraction orders because of their enhancement of the scattering intensity for the diffraction waves. The distributions of the real part of E_z are summarized in Fig. 4e–g for $a_\parallel$ = 800, 850 and 900 nm. We can see that when $\lambda^{sup}_{(\pm1,\ 0)}$ moves towards the resonance wavelength of the D_1 mode, the coupling strength between $\lambda^{sup}_{(\pm1,\ 0)}$ and the D_1 mode becomes stronger and the two lobes of E_z are pushed towards the "hot spots" at the bottom of the NCs, which confirms the co-coupling of D_1 and D_2 modes with $\lambda^{sup}_{(\pm1,\ 0)}$. This co-coupling behavior is attributed to the wavelength overlap between the D_1 and D_2 modes, *i.e.*, both the D_1 and D_2 modes are able to enhance the scattering intensity of the diffraction waves when their resonance wavelengths overlap with $\lambda^{sup}_{(\pm1,\ 0)}$.

To further study the co-coupling behavior, we modify the NCA structure by removing the bottom part of the Au shell, as shown in Fig. 5a. Δh = 100 nm was set to suppress the effect of the substrate on the D_1 mode. Fig. 5b shows the transmission spectra of this modified structure with h = 400 nm and $a_\perp$ = 400 nm. Fig. S2 in the ESI† shows the transmission spectra for the modified structures with h = 150, 200, and 300 nm. Since the "hot spots" of the D_1 mode are separated from the substrate, a blueshift of the resonance wavelength for the D_1 mode and a weakened coupling between $\lambda^{sub}_{(\pm1,\ 0)}$ and the D_1 mode is observed. The evolution of the real part of E_z with different lattice constants ($a_\parallel$ = 750, 800, and 900 nm, respectively) is displayed in Fig. 5c–e. When $\lambda^{sup}_{(\pm1,\ 0)}$ is close to the resonance wavelength of the D_2 mode, the plasmonic–photonic coupling between these two modes is strong and the coupling between $\lambda^{sup}_{(\pm1,\ 0)}$ and the D_1 mode is weak. The increase of $a_\parallel$ enhances the coupling between $\lambda^{sup}_{(\pm1,\ 0)}$ and the D_1 mode, and reduces the coupling between $\lambda^{sup}_{(\pm1,\ 0)}$ and the D_2 mode.

Refractive index sensing in the core/shell NCAs

The near-field distributions of the Q and D_2 modes suggest that the "hot spots" of these two height-induced LSPRs are located away from the substrate, revealing the potential for a narrower linewidth in the LPRs to enhance the FOM of plasmonic sensors. In addition, the co-coupling behavior of the D_2 and the D_1 mode implies that we can tune the lattice constant $a_\parallel$ to strengthen the coupling between the D_2 mode and $\lambda^{sup}_{(\pm1,\ 0)}$ and suppress the effect of the substrate. The sensing perform-

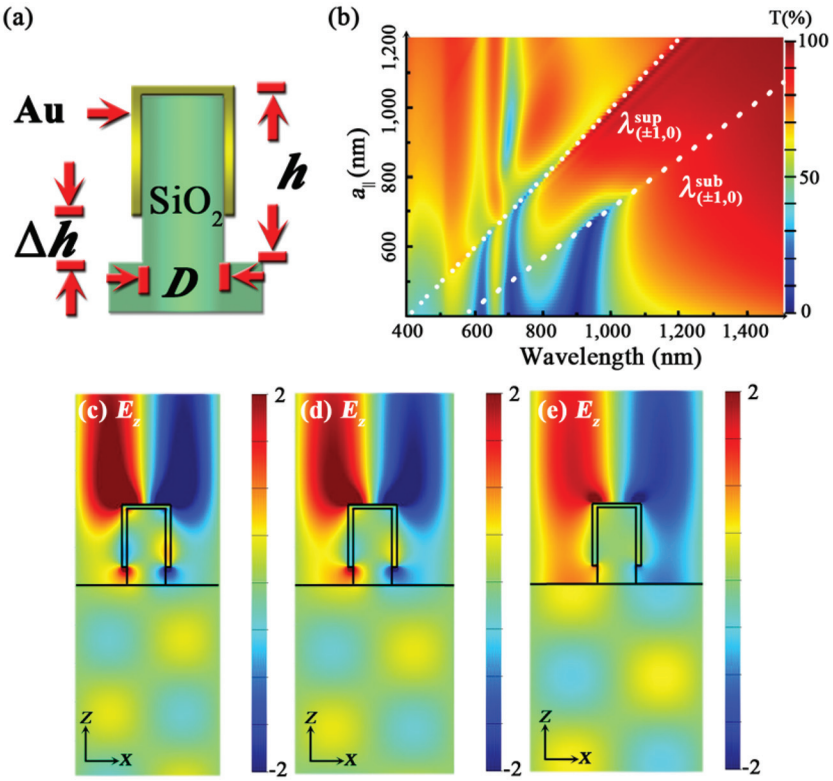

Fig. 5 (a) Cross section of the modified core/shell NC with the bottom part of the Au nanoshell removed, the distance between the bottom of the Au nanoshell and the SiO_2 substrate is indicated as Δh, which is 100 nm. (b) Transmission spectra of the modified NCAs as a function of $a_{\parallel}$. The NCAs have D = 200 nm, h = 400 nm and $a_{\perp}$ = 400 nm. (c)–(e) Distributions of the real part of E_z in the xz plane through the center of the NCs. The NCAs have (c) $a_{\parallel}$ = 750 nm, λ = 752 nm, (d) $a_{\parallel}$ = 800 nm, λ = 796 nm, (e) $a_{\parallel}$ = 900 nm, λ = 880 nm.

ances based on the core/shell SiO_2/Au NCAs are summarized in Fig. 6. Firstly, we examine the sensing performance of the SiO_2/Au NCAs with a low aspect ratio, which, however, could be optimized to achieve high FOM in a quasi-symmetric environment. We take the NCAs with h = 100 nm, $a_{\perp}$ = 400 nm, and $a_{\parallel}$ = 600 nm as an exemplary structure. Fig. 6a shows the transmission spectra as a function of the superstrate refractive index, which ranges from 1.0 to 1.5. The D_2 mode is weak when h = 100 nm (also see Fig. 3b). For a lower refractive index, $\lambda^{sup}_{(\pm1,\ 0)}$ is away from the resonance wavelength of the D_1 mode and the coupling is also weak. However, when the refractive index reaches 1.4, a narrow and sharp transmission dip is observed. This resonance dip with a high quality factor is attributed to the wavelength matching between $\lambda^{sup}_{(\pm1,\ 0)}$ and the D_1 mode in a quasi-symmetric environment. The FWHM of <10 nm is estimated based on the spectrum with a refractive index of 1.5. Considering that the refractive index ranges from 1.4 to 1.5, a high FOM of 59 is achieved. This is consistent with the previously reported LPR-based plasmonic sensors, which exhibited high FOMs when the refractive index of the target analyte was close to that of the substrate. However, the core/shell SiO_2/Au NCAs show a much higher FOM than that reported in the square or hexagonal Au nanoparticle arrays.[44,48] It should be noted that LPR is a coupling mode, which requires a good wavelength matching between the LSPRs and the diffraction orders to achieve a high quality factor. Since the wavelength sensitivity of the LSPRs to the refractive index of the target analyte is quite different from that of the diffraction orders, the change of the refractive index will lead to a deviation between the plasmonic mode and the photonic mode, resulting in a weak coupling and a low FOM. This explains why the detected range of the analyte refractive index is limited in the conventional LPR-based plasmonic sensors. To our benefit, optimization of the aspect ratio in the core/shell NCAs provides a mechanism to maintain the high FOM for a wide range of the analyte refractive indices.

Fig. 6b shows the sensing performance of the core/shell NCAs with $a_{\perp}$ = 400 nm, $a_{\parallel}$ = 650 nm, and h = 400 nm. Compared with the results in the Au NDAs, a narrower linewidth and a concomitant higher FOM are obtained. To clearly demonstrate the spectral shift of the LPR dips, we have plotted the normalized transmission spectra in Fig. 6c. As shown in Fig. 3e, $\lambda^{sup}_{(\pm1,\ 0)}$ is able to couple with the Q, D_1 and D_2 modes, respectively, when it crosses over the spectral region of these LSPRs. This is the basic concept we employ to maintain the high FOM over a wide range of analyte refractive index. The narrow linewidth at around 700 nm indicates the coupling between $\lambda^{sup}_{(\pm1,\ 0)}$ and the Q mode. The linewidth at a refractive index of 1.1 is much broader than that in other transmission dips because $\lambda^{sup}_{(\pm1,\ 0)}$ at 715 nm weakly couples with the Q mode

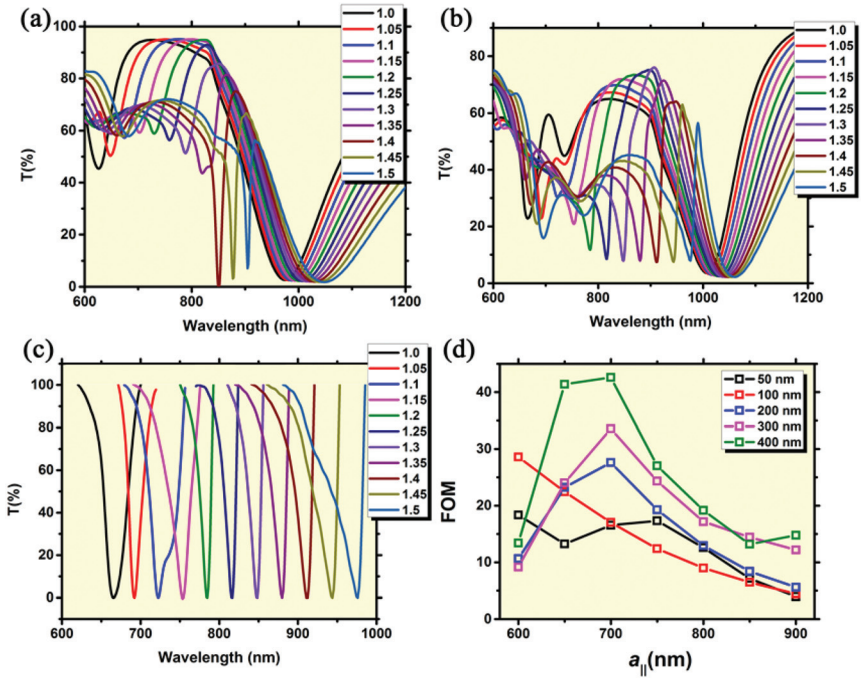

Fig. 6 (a) and (b) Transmission spectra of the core/shell SiO_2/Au NCAs as a function of the superstrate refractive index, which ranges from 1.0 to 1.5. The NCAs have D = 200 nm, $a_{\perp}$ = 400 nm and (a) $a_{||}$ = 600 nm, h = 100 nm, (b) $a_{||}$ = 650 nm, h = 400 nm. (c) Normalized transmission dips of the LPRs in (b). (d) FOM for the core/shell SiO_2/Au NCAs with D = 200 nm, $a_{\perp}$ = 400 nm and h = 50, 100, 200, 300 and 400 nm as a function of $a_{||}$.

(a small dip shown in Fig. 6c) and cannot couple with the D_2 mode. The narrow dips from 750 nm to 900 nm derive from the coupling between $\lambda^{sup}_{(\pm1,\ 0)}$ and the D_2 mode, which is much stronger than the coupling between $\lambda^{sup}_{(\pm1,\ 0)}$ and the D_1 mode, and suppressing the effect of the substrate. Further increase of the refractive index will slightly increase the linewidth as the coupling between $\lambda^{sup}_{(\pm1,\ 0)}$ and the D_1 mode becomes dominant. Compared with the LPR-based plasmonic sensors reported previously, the core/shell NCAs with a high aspect ratio show tremendous advantage for the development of plasmonic sensors with a wide working range of refractive index.

To summarize the sensing performance, the FOM for the core/shell SiO_2/Au NCAs with different aspect ratios as a function of $a_{||}$ is shown in Fig. 6d. Since the FWHM depends on the superstrate refractive index, we calculate the FWHM at a refractive index of 1.2. Although the NCAs with a low aspect ratio (h = 50 or 100 nm) have a high FOM of ~20 or 30 at $a_{||}$ = 600 nm, the extinction efficiency is rather low for these structures, indicating a low SNR for plasmonic sensors. The SNR can be significantly improved when $a_{||}$ is increased, but the broadening of the linewidth leads to a lower FOM. The higher FOM is obtained in the high aspect ratio structures, with the highest FOM of 42.6 achieved when $a_{||}$ = 700 nm and h = 400 nm. Although this FOM is lower than the highest FOM (~108) in the LPR-based plasmonic sensors reported so far,[45] the much higher SNR and the broad working range of the analyte refractive index make our structures promising for practical applications.

Conclusions

The parallel palsmonic–photonic couplings in both the Au NDAs and the core/shell SiO_2/Au NCAs are studied. Different from the dipolar interaction in orthogonal coupling, the horizontally propagating electric field in the diffracted waves leads to the generation of out-of-plane "hot spots" and the delocalization of the electric field intensity. Moreover, the engineering of the near field "hot spots" through controlling the aspect ratio in the NCAs leads to the parallel coupling between height-induced LSPRs and the superstrate diffraction orders, which provides great opportunity to develop high-performance on-chip plasmonic sensors. Specifically, with the increase of the aspect ratio, both high FOM and SNR could be achieved over a wide working range of refractive indices (1.0 to 1.5) for the target analyte. The proposed core/shell SiO_2/Au NCAs can be fabricated by selective chemical deposition of the Au layer on the SiO_2 NCAs with a photoresist to protect the substrate between the neighboring SiO_2 NCs. E-beam lithography can be applied to fabricate the SiO_2 NCAs. The photoresist will be removed by a lift-off process after the Au deposition. This design of on-chip plasmonic sensors will facilitate its widespread applications in label-free chemical or biomedical detection.

Acknowledgements

The authors acknowledge the financial support of the Beckman Young Investigator Program and the Texas Advanced

Computing Center (TACC) at The University of Texas at Austin for providing HPC resources that have contributed to the research results reported within this paper. URL: http://www.tacc.utexas.edu. We thank B. Bangalore Rajeeva, X. Peng, M. Wang, and Z. Wu for helpful discussions on the simulation results and proofreading the manuscript.

Notes and references

1 K. Tanaka, E. Plum, J. Y. Ou, T. Uchino and N. I. Zheludev, *Phys. Rev. Lett.*, 2010, **105**, 227403.
2 N. Gandra, C. Portz, L. Tian, R. Tang, B. Xu, S. Achilefu and S. Singamaneni, *Angew. Chem., Int. Ed.*, 2014, **53**, 866–870.
3 D. Lu, J. J. Kan, E. E. Fullerton and Z. Liu, *Nat. Nanotechnol.*, 2014, **9**, 48–53.
4 X. Dang, J. Qi, M. T. Klug, P.-Y. Chen, D. S. Yun, N. X. Fang, P. T. Hammond and A. M. Belcher, *Nano Lett.*, 2013, **13**, 637–642.
5 O. Neumann, C. Feronti, A. D. Neumann, A. Dong, K. Schell, B. Lu, E. Kim, M. Quinn, S. Thompson, N. Grady, P. Nordlander, M. Oden and N. J. Halas, *Proc. Natl. Acad. Sci. U. S. A.*, 2013, **110**, 11677–11681.
6 S. Mubeen, J. Lee, W.-r. Lee, N. Singh, G. D. Stucky and M. Moskovits, *ACS Nano*, 2014, **8**, 6066–6073.
7 H. A. Atwater and A. Polman, *Nat. Mater.*, 2010, **9**, 205–213.
8 Y. B. Zheng, B. Kiraly, P. S. Weiss and T. J. Huang, *Nanomedicine*, 2012, **7**, 751–770.
9 Y. B. Zheng, J. L. Payton, T.-B. Song, B. K. Pathem, Y. Zhao, H. Ma, Y. Yang, L. Jensen, A. K. Y. Jen and P. S. Weiss, *Nano Lett.*, 2012, **12**, 5362–5368.
10 L. Scarabelli, M. Coronado-Puchau, J. J. Giner-Casares, J. Langer and L. M. Liz-Marzán, *ACS Nano*, 2014, **8**, 5833–5842.
11 K. A. Willets and R. P. Van Duyne, *Annu. Rev. Phys. Chem.*, 2007, **58**, 267–297.
12 C. Zhao, Y. Liu, J. Yang and J. Zhang, *Nanoscale*, 2014, **6**, 9103–9109.
13 L. L. Zhao, L. Jensen and G. C. Schatz, *Nano Lett.*, 2006, **6**, 1229–1234.
14 W. Wan, W. Zheng, Y. Chen and Z. Liu, *Nanoscale*, 2014, **6**, 9093–9102.
15 L. Shao, Q. Ruan, R. Jiang and J. Wang, *Small*, 2014, **10**, 802–811.
16 L. Tong, H. Wei, S. Zhang and H. Xu, *Sensors*, 2014, **14**, 7959–7973.
17 H. Wei and H. Xu, *Nanoscale*, 2013, **5**, 10794–10805.
18 R. Bardhan, S. Lal, A. Joshi and N. J. Halas, *Acc. Chem. Res.*, 2011, **44**, 936–946.
19 C. Ayala-Orozco, C. Urban, M. W. Knight, A. S. Urban, O. Neumann, S. W. Bishnoi, S. Mukherjee, A. M. Goodman, H. Charron, T. Mitchell, M. Shea, R. Roy, S. Nanda, R. Schiff, N. J. Halas and A. Joshi, *ACS Nano*, 2014, **8**, 6372–6381.
20 T. Klar, M. Perner, S. Grosse, G. von Plessen, W. Spirkl and J. Feldmann, *Phys. Rev. Lett.*, 1998, **80**, 4249–4252.
21 R. Bukasov, T. A. Ali, P. Nordlander and J. S. Shumaker-Parry, *ACS Nano*, 2010, **4**, 6639–6650.
22 N. J. Halas, S. Lal, W. S. Chang, S. Link and P. Nordlander, *Chem. Rev.*, 2011, **111**, 3913–3961.
23 K. H. Fung, A. Kumar and N. X. Fang, *Phys. Rev. B: Condens. Matter*, 2014, **89**, 045408.
24 E. Prodan, C. Radloff, N. J. Halas and P. Nordlander, *Science*, 2003, **302**, 419–422.
25 B. Auguie and W. L. Barnes, *Phys. Rev. Lett.*, 2008, **101**, 143902.
26 Y. Chu, E. Schonbrun, T. Yang and K. B. Crozier, *Appl. Phys. Lett.*, 2008, **93**, 181108.
27 V. G. Kravets, F. Schedin and A. N. Grigorenko, *Phys. Rev. Lett.*, 2008, **101**, 087403.
28 H. Gao, J. M. McMahon, M. H. Lee, J. Henzie, S. K. Gray, G. C. Schatz and T. W. Odom, *Opt. Express*, 2009, **17**, 2334–2340.
29 A. Vitrey, L. Aigouy, P. Prieto, J. M. García-Martín and M. U. González, *Nano Lett.*, 2014, **14**, 2079–2085.
30 A. G. Nikitin, T. Nguyen and H. Dallaporta, *Appl. Phys. Lett.*, 2013, **102**, 221116.
31 A. G. Nikitin, *Appl. Phys. Lett.*, 2014, **104**, 061107.
32 L. Lin and Y. Yi, *Opt. Lett.*, 2014, **39**, 4823–4826.
33 L. Lin and Y. Zheng, *Opt. Lett.*, 2015, **40**, 2060–2063.
34 V. A. Markel, *J. Mod. Opt.*, 1993, **40**, 2281–2291.
35 S. L. Zou, N. Janel and G. C. Schatz, *J. Chem. Phys.*, 2004, **120**, 10871–10875.
36 S. L. Zou and G. C. Schatz, *J. Chem. Phys.*, 2004, **121**, 12606–12612.
37 V. A. Markel, *J. Phys. B: At., Mol. Opt. Phys.*, 2005, **38**, L115–L121.
38 M. Meier, A. Wokaun and P. F. Liao, *J. Opt. Soc. Am. B*, 1985, **2**, 931–949.
39 L. L. Zhao, K. L. Kelly and G. C. Schatz, *J. Phys. Chem. B*, 2003, **107**, 7343–7350.
40 J. Y. Suh, C. H. Kim, W. Zhou, M. D. Huntington, D. T. Co, M. R. Wasielewski and T. W. Odom, *Nano Lett.*, 2012, **12**, 5769–5774.
41 F. van Beijnum, P. J. van Veldhoven, E. J. Geluk, M. J. A. de Dood, G. W. t. Hooft and M. P. van Exter, *Phys. Rev. Lett.*, 2013, **110**, 206802.
42 W. Zhou, M. Dridi, J. Y. Suh, C. H. Kim, D. T. Co, M. R. Wasielewski, G. C. Schatz and T. W. Odom, *Nat. Nanotechnol.*, 2013, **8**, 506–511.
43 J. Henzie, M. H. Lee and T. W. Odom, *Nat. Nanotechnol.*, 2007, **2**, 549–554.
44 A. I. Kuznetsov, A. B. Evlyukhin, M. R. Goncalves, C. Reinhardt, A. Koroleva, M. L. Arnedillo, R. Kiyan, O. Marti and B. N. Chichkov, *ACS Nano*, 2011, **5**, 4843–4849.
45 Y. Shen, J. Zhou, T. Liu, Y. Tao, R. Jiang, M. Liu, G. Xiao, J. Zhu, Z.-K. Zhou, X. Wang, C. Jin and J. Wang, *Nat. Commun.*, 2013, **4**, 2381.
46 B. Spackova and J. Homola, *Opt. Express*, 2013, **21**, 27490–27502.
47 Y. Du, L. Shi, M. Hong, H. Li, D. Li and M. Liu, *Opt. Commun.*, 2013, **298**, 232–236.

48 P. Offermans, M. C. Schaafsma, S. R. K. Rodriguez, Y. Zhang, M. Crego-Calama, S. H. Brongersma and J. G. Rivas, *ACS Nano*, 2011, **5**, 5151–5157.
49 B. Auguie, X. M. Bendana, W. L. Barnes and F. J. Garcia de Abajo, *Phys. Rev. B: Condens. Matter*, 2010, **82**, 155447.
50 K. M. Mayer and J. H. Hafner, *Chem. Rev.*, 2011, **111**, 3828–3857.
51 K. A. Tetz, L. Pang and Y. Fainman, *Opt. Lett.*, 2006, **31**, 1528–1530.
52 L. Lin and Y. Yi, *Opt. Express*, 2015, **23**, 130–142.
53 L. J. Sherry, S. H. Chang, G. C. Schatz, R. P. Van Duyne, B. J. Wiley and Y. N. Xia, *Nano Lett.*, 2005, **5**, 2034–2038.
54 A. Dmitriev, C. Hägglund, S. Chen, H. Fredriksson, T. Pakizeh, M. Käll and D. S. Sutherland, *Nano Lett.*, 2008, **8**, 3893–3898.